




# Perovskite solar cell technology scaling-up: Eco-efficient and industrially compatible sub-module manufacturing by fully ambient air slot-die/blade meniscus coating

Luigi Vesce<sup>1</sup>  | Maurizio Stefanelli<sup>1</sup> | Federico Rossi<sup>2,3</sup> |  
 Luigi Angelo Castriotta<sup>1</sup> | Riccardo Basosi<sup>2,3,4</sup>  | Maria Laura Parisi<sup>2,3,4</sup> |  
 Adalgisa Sinicropi<sup>2,3,4</sup>  | Aldo Di Carlo<sup>1,5</sup>

<sup>1</sup>CHOSE, Centre for Hybrid and Organic Solar Energy, Department of Electronic Engineering, University of Rome "Tor Vergata", Rome, Italy

<sup>2</sup>Department of Biotechnology, Chemistry and Pharmacy, R<sup>2</sup>ES Lab, University of Siena, Siena, Italy

<sup>3</sup>CSGI, Center for Colloid and Surface Science, Florence, Italy

<sup>4</sup>ICCOM-CNR, Institute for the Chemistry of Organo Metallic Compounds, National Research Council, Florence, Italy

<sup>5</sup>ISM-CNR, Institute of Structure of Matter, National Research Council, Rome, Italy

## Correspondence

Aldo Di Carlo, CHOSE, Centre for Hybrid and Organic Solar Energy, Department of Electronic Engineering, University of Rome "Tor Vergata", Via del Politecnico 1, 00133 Rome, Italy.

Email: [aldo.dicarlo@uniroma2.it](mailto:aldo.dicarlo@uniroma2.it)

## Funding information

Horizon Europe Framework Programme, Grant/Award Number: 101084124; Horizon 2020 Framework Programme, Grant/Award Numbers: 881603, 826013, 764047

## Abstract

The efficiency gap between perovskite (PVSK) solar sub-modules (size  $\geq 200$  cm<sup>2</sup>) and lab scale cells (size  $< 1$  cm<sup>2</sup>) is up to 36%. Moreover, the few attempts present in the literature used lab-scale techniques in a glove-box environment, reducing its compatibility for further product industrialization. Here, we report a PVSK sub-module (total area 320 cm<sup>2</sup>, aperture area 201 cm<sup>2</sup>, 93% geometrical fill factor [GFF]) fabricated in ambient air by hybrid meniscus coating techniques assisted by air and green antisolvent quenching method. To suppress nonradiative recombination losses, improve carrier extraction and control the PVSK growth on such a large surface, we adopted phenethylammonium iodide (PEAI) passivation and PVSK solvent addiction strategies. The high homogeneous and reproducible layers guarantee an efficiency of 16.13% (7% losses with respect to the small area cell and zero losses with respect to the mini-modules) and a stability of more than 3000 h according to International Summit on Organic PV Stability, dark storage/shelf life in ambient (ISOS-D-1). The sustainability of used methods and materials is demonstrated by the life cycle assessment. The scale-up operation allows for strong impact mitigation in all the environmental categories and more efficient consumption of the resources. Finally, the economic assessment shows a strong cost reduction scaling from mini- to sub-module (about 40%).

## KEYWORDS

ambient air meniscus coating, life cycle assessment, life cycle costing, passivation, perovskite solar cells, process engineering, stability, sub-module scaling-up

## 1 | INTRODUCTION

The solution process photovoltaic (PV) technology developed by organometal halide perovskite (PVSK) solar cells (PSCs) and the peculiar

physical/chemical properties delivered power conversion efficiencies higher than any thin film.<sup>1–4</sup> The efforts related to the material compositions, the device architecture, and the fabrication process permitted to reach efficiencies of up to 26.1% for the single junction and 33.7% in tandem with silicon. The real exploitation at the market level of PVSK PV technology can be feasible only if the laboratory cells

Luigi Vesce and Maurizio Stefanelli, both authors, contributed equally to this work.

This is an open access article under the terms of the [Creative Commons Attribution](https://creativecommons.org/licenses/by/4.0/) License, which permits use, distribution and reproduction in any medium, provided the original work is properly cited.

© 2023 The Authors. Progress in Photovoltaics: Research and Applications published by John Wiley & Sons Ltd.

(area  $<1\text{ cm}^2$ ) results will be transferred to mini (area  $<200\text{ cm}^2$ ) and sub-module devices ( $200\text{ cm}^2 \leq \text{area} \leq 800\text{ cm}^2$ ).<sup>1,5-7</sup> A module device is composed of a number of sub-cells connected in series to overcome the non-negligible sheet resistance of the transparent conductive oxide (TCO) glass substrates that induce large ohmic losses when the current of the cell increases.<sup>8</sup> In the scaling-up route, the high-quality large area PVSK films, the low losses induced by front contact and the cells' interconnections are the main factors in getting reproducible and reliable high-efficiency modules.<sup>7,9-11</sup> Layers inhomogeneity rises when transferring to module devices processes and material compositions optimized for the small area cells.<sup>12</sup> In the case of the polycrystalline nature of the solution-processed PVSK layers, defects at grain boundaries and vacancies during the fabrication process can occur.<sup>13</sup>

The efforts devoted to scaling up the PSC technology to mini-module size led to the identification of different strategies able to maximize efficiency both in the nitrogen air glove box and ambient air environment. In the first case, the doctor-blading technique and a subsequent antisolvent (diethylether) bath were used on a  $9\text{ cm}^2$  active area module to deposit  $\text{MAFAPbI}_3$  PVSK with an efficiency of 17.9%.<sup>14</sup> Bu et al. obtained 19.3% efficiency on a slot-die coated Formamidinium (FA)-based PVSK n-i-p module ( $17.1\text{ cm}^2$  active area) by forming a stable  $\text{PbI}_2 \bullet \text{N}$ -methylpyrrolidone (NMP) adduct.<sup>15</sup> Liu et al. demonstrated that o-PDEAl<sub>2</sub> is an effective passivation agent to reach 21.4% (10% loss from small area cell) efficient PVSK solar mini-module ( $26\text{ cm}^2$  active area) by spin coating technique.<sup>16</sup> Vesce et al. demonstrated an efficiency of 19.1% (8% loss from small area cell) for a low-temperature planar n-i-p PVSK module ( $11\text{ cm}^2$  aperture area, 91% aspect ratio) by avoiding dimethyl sulfoxide (DMSO) detrimental effect and by PEAl defect passivation.<sup>11</sup> Recently, Ding et al. reported an efficiency of 22.72% on a  $24\text{ cm}^2$  active area by spin coating technique and introducing a facile solvothermal method to synthesize single-crystalline  $\text{TiO}_2$  rhombohedral nanoparticles.<sup>17</sup> Han et al. reported a spin-coated module ( $100\text{ cm}^2$  aperture area and  $95.5\text{ cm}^2$  active area) with an efficiency on the active area of 14% by an electrostatic self-assembly method to deposit the  $\text{SnO}_2$  electron transporting layer (ETL).<sup>18</sup> In the nitrogen glove box, further attempts to enlarge the mini-module area led to efficiency on active area of 13.4% ( $108\text{ cm}^2$  active area,  $122.73\text{ cm}^2$  aperture area) and 11.1% ( $151.88\text{ cm}^2$  active area,  $168.75\text{ cm}^2$  aperture area) by spin-coated  $\text{MAPbI}_3$  PVSK and slot-die coated  $\text{CsMAFA}$  PVSK, respectively.<sup>19,20</sup>

In ambient air, Deng et al. reported the blade coating method to deposit  $\text{MAPbI}_3$  and FACs PVSK p-i-n mini-module with an efficiency of 19.1% and 20.2, respectively.<sup>21,22</sup> Chen et al. reached 20.1% power conversion efficiency (PCE) on  $16.4\text{ cm}^2$  active area p-i-n module by blade coating deposition technique at room temperature and by partially replacing DMSO with solid-state carbonylazide in  $\text{MAFAPbI}_3$  PVSK.<sup>23</sup> Du et al. fabricated a slot-die coated n-i-p mini-module ( $10.2\text{ cm}^2$  active area) with 18.6% efficiency by ionic liquid passivation of the  $\text{CsMAFA}$  PVSK surface defects.<sup>24</sup> Blade-coating deposition method was adopted with  $\text{MAPbI}_3$  PVSK by thermal assistance (p-i-n module)<sup>25</sup> and gas quenching<sup>26-28</sup> reaching the maximum efficiency

of 14.9% on a  $57.8\text{ cm}^2$  aperture area. An efficiency of 16.1% on a  $16\text{ cm}^2$  active area was obtained by applying potassium-doped graphene oxide as interlayer and infrared annealing of the  $\text{CsFA}$  PVSK.<sup>29</sup> Vesce et al. reported an air-assisted blade-coating method to deposit the full stack of an n-i-p  $32\text{ cm}^2$  module device ( $11\text{ cm}^2$  aperture area) in ambient air with an efficiency of 16.1% (6% loss from small area cell).<sup>5</sup> Besides the efforts on mini-modules, the development of scaled-up manufacturing processes for PVSK solar sub-modules is crucial to provide an expeditious and economical transition into mass production of such devices as PVSK solar panels and arrays.<sup>9</sup> In 2018, Toshiba fabricated a planar p-i-n  $703\text{ cm}^2$  sub-module with an efficiency of 11.7% by applying meniscus printing technology.<sup>6,30</sup> The device was prepared on a resin film fixed on a glass plate and then sealed with a second glass plate. Recently, Bu et al. reported 15.3% efficiency on  $205\text{ cm}^2$  module by blade-coated FACs PVSK with methylammonium chloride additives in the glovebox, but with high losses with respect to small-sized cell (more than 36%) and mini-module (more than 25%).<sup>31</sup>

In summary, several coating/printing methods have been investigated for scaling up different PVSK compounds both in the glove box and ambient air environment.<sup>7</sup> For each method, proper optimizations of PVSK precursor solution and deposition parameters are mandatory to produce highly efficient and stable devices. The quality of a coating and the related defects depend on the deposition conditions and the ink rheology (surface tension and viscosity).<sup>32-34</sup> Despite big efforts in the scaling up of PVSK technology in literature, few works faced sub-module fabrication for different reasons. First of all, the spin coating technique, which is still widely used for the fabrication of mini-modules, cannot be considered a scalable deposition method and usually requires intense manual practice to produce a uniform coating without pin holes.<sup>27,35</sup> Moreover, processes realized in a glove box are costly with respect to ambient air and not replicable in a real plant.<sup>9,36</sup> Finally, the manufacturing process should achieve some fundamental requirements: environmentally sustainable, low cost, reliable and high throughput production, good performance, and stability of the device.<sup>8,37-40</sup> About the first point, life cycle assessment (LCA) is an effective and very powerful methodology to perform sustainability evaluation, particularly for energy conversion technologies.<sup>41</sup> The LCA analytical approach allows for outlining the environmental footprint of the investigated system by calculating emissions and releases to the environment of the whole product or process value chain.<sup>40</sup> Since LCA has been hugely applied to assess PV technologies,<sup>42</sup> there is a general consensus that attributional LCA is the best approach to study emerging technologies at small-scale production when robust primary data are available.<sup>43-46</sup> LCA studies of PVSK devices are present in the literature highlighting the importance of improving the scalability of manufacturing processes to achieve competitive environmental performances.<sup>40,47,48</sup> Moreover, Zhang et al. performed an integrated sustainability assessment of PVSK cells based on secondary data from other literature studies.<sup>49</sup> From the economic perspective, the manufacturing cost of the PSCs can vary in a very wide range ( $37\text{--}257\text{ \$/m}^2$ ) as a function of the selected materials and manufacturing techniques.<sup>50</sup> On the other hand, Song et al. have proposed a

scenario-based prospective assessment where large modules will be produced on a large scale; accordingly, their manufacturing cost is estimated to be 31.7 \$/m<sup>2</sup>.<sup>50</sup>

As shown, the PCE of PVSK PVs decreases as the active area of the devices increases regardless of fabrication processes.<sup>9,35</sup> In this work, we show the scaling up of PSC technology till the sub-module size (320 cm<sup>2</sup> total area, 201 cm<sup>2</sup> aperture area, 186.1 cm<sup>2</sup> active area) by a hybrid (blade/slot-die coating) meniscus coating process out of glovebox with green antisolvent quenching. PVSK passivation and acetonitrile (ACN) solvent addition were introduced to suppress nonradiative recombination losses and control nuclei formation, respectively. To the best of our knowledge, this is the first time that a sub-module was fabricated outside the glovebox by scalable deposition techniques. The demonstrated homogeneity of the full stack permitted it to reach a record efficiency of 16.13% (7% losses with respect to small area cell, 93% geometrical fill factor [GFF]) and stabilized efficiency at 1 SUN maximum power point (MPP) of 15.5%. The performance is equal to the blade-coated mini-module fabricated in our recent publication.<sup>5</sup> The sub-module was stable at the ISOS-D-1 test for more than 3000 h. Furthermore, LCA is employed to demonstrate the economic and environmental advantages deriving from the module's scale-up. Different from previous studies based on future industrial-level scenarios, and according to our knowledge, this work presents the first LCA focusing on the potential benefits of PVSK devices scaling up process grounding on primary data derived from experimental tests. Therefore, the goal of this analysis is not to evaluate the economic and environmental competitiveness of the proposed production line compared to the state-of-the-art results published in the literature. Rather, the aim is to provide a detailed description of the mini-module and sub-module eco-profiles manufactured via a hybrid blade/slot-die coating method along with a discussion of the highly representative results concerning the hotspots and advantages characterizing the fine-tuned process. Moreover, we document that the scaled antisolvent washing does not represent a critical issue for the economic and environmental sustainability of the scale-up operation.

## 2 | RESULTS AND DISCUSSION

### 2.1 | Process and chemical engineering of PVSK sub-module

The aim of this work is to demonstrate the scaling-up in ambient air from small area cells to mini- and sub-module sizes with low-efficiency loss. The reference n-i-p mini-module is reported in our recent work, where we showed an efficiency of 16.1% on 10 cm<sup>2</sup> active area (five series connected cells, 11 cm<sup>2</sup> aperture area, 32 cm<sup>2</sup> total area).<sup>5</sup> Here, the full stack formed by ETL, PVSK and hole transporting layer (HTL) was coated by scalable deposition techniques (spray and blade coating) in ambient air (25°C, 30% RH). The CsMAFA triple cation PVSK deposition process was based on the following procedure. After the meniscus formation, the blade-coating machine (Charon, Cicci Research) deposits the loaded material assisted by a heated dry airflow to reach the supersaturated state of the PVSK film. A subsequent 2-propanol (isopropyl alcohol [IPA]) antisolvent quenching is performed by the same deposition method to remove the DMSO excess and force crystallization of PVSK, because of 2-propanol lower boiling point and high viscosity compared to DMSO.<sup>51</sup> Then the substrate is annealed at 100°C for 40 min to allow the PVSK to grow.<sup>52</sup> We further scaled up the device to a sub-module size of 320 cm<sup>2</sup>, composed of 16 series connected cells with active and aperture areas of 186.1 and 201 cm<sup>2</sup> (93% GFF), respectively. The P1 (TCO patterning), P2 (ablation of PVSK and transport layers), and P3 (selective removal of counter-electrode) laser patterning steps are realized by a nano-second UV laser system (see Sections 2.2 and 4) (Figure 1A). We used the planar PSC structure composed of fluorine-doped tin oxide (FTO)-covered glass and a slot-die-coated SnO<sub>2</sub> layer (Figure 1A). On top, the CsMAFA PVSK solution was deposited via the blade coating technique described above. The full process is at a low temperature (150°C max for ETL annealing) and out of glove box.

First, we tested the planar structure on 0.5 cm<sup>2</sup> active area cells, fabricated on a 32 cm<sup>2</sup> substrate. The current density–voltage curve

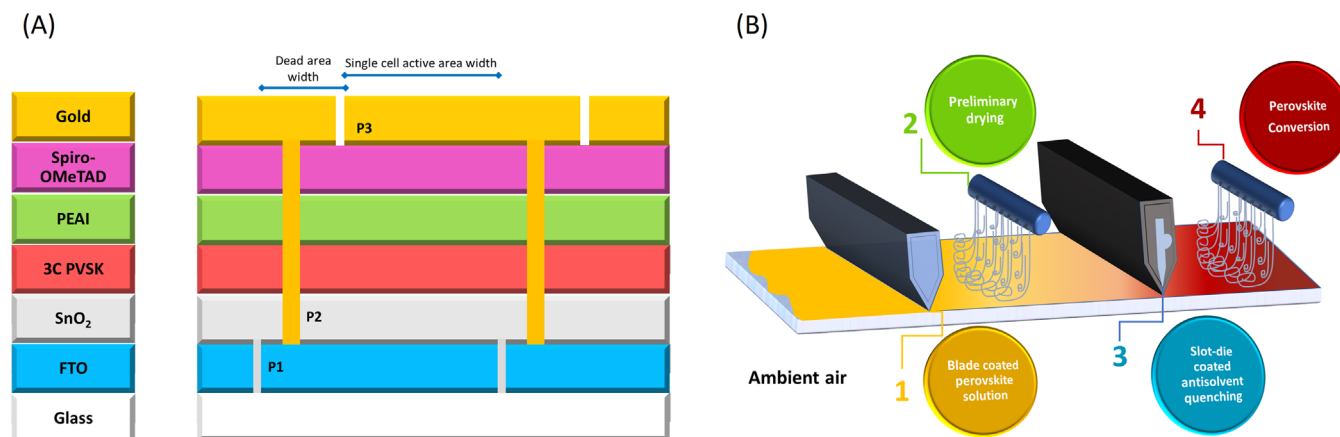


**FIGURE 1** (A) Scheme of the n-i-p module architecture and of the P1 P2 P3 interconnection. (B) Perovskite (PVSK) deposition process by blade/slot-die coating technique in ambient air. [Colour figure can be viewed at [wileyonlinelibrary.com](https://onlinelibrary.wiley.com/doi/10.1002/pip.3741)]

of the champion cell shows a short-circuit current density ( $J_{sc}$ ) of 20.40 mA/cm<sup>2</sup>, an open circuit voltage ( $V_{oc}$ ) of 1.15 V, and a fill factor (FF) of 73% for a record PCE of 17.08% (Figure 2A). As already demonstrated in our recent publication,<sup>5</sup> cells fabricated by spin coating technique in the glove box (nitrogen atmosphere) on a 2.5 cm<sup>2</sup> × 2.5 cm<sup>2</sup> substrates got similar results:  $J_{sc}$  = 20.54 mA/cm<sup>2</sup>,  $V_{oc}$  = 1.14 V, FF = 72.32%, and PCE = 17.05% (Figure 2A). Figure S1 shows the higher reproducibility of six fabricated cells by the blade coating method with respect to the spin coating method (4% vs. 6% standard deviation).

Then, we transferred the process optimized for 32 cm<sup>2</sup> to the 320 cm<sup>2</sup> substrate by adjusting the materials amount (see Section 4) accordingly. The efficiency was 7.92% with  $V_{oc}$  = 15.65 V,  $I_{sc}$  = 139.56 mA,  $J_{sc}$  = 12 mA/cm<sup>2</sup>, and FF = 63.18% (Figure 2B). The most affected parameter was the current because of the poor DMSO washing during the isopropanol air-assisted blade-coating deposition. It is easy to understand that the loaded isopropanol amount forming the meniscus between the blade and the substrate does not guarantee the full coverage of the large substrate for two reasons. First, the solvent penetrates in the PVSK layer to wash DMSO. Moreover, during the process, the airflow fosters the evaporation rate of the low boiling solvent before reaching the end of the substrate by affecting the meniscus shape.<sup>9</sup> Chen et al. recently demonstrated how DMSO trapping and sticking during film formation formed voids at the PVSK-substrate interface when DMSO escapes.<sup>23</sup> We solved this issue by continuously refilling the meniscus with the slot-die coating method (Figures S2 and 1B). Here, the solvent is dispersed from a tank through a feed slot between two dies.<sup>53,54</sup> The isopropanol washing efficacy can be kept during the full process by a continuous flow rate forming a steady state meniscus.<sup>9,35,55</sup> Obviously, the height of the slot-die head, material amount, and dispensing rate are optimized. The synergic effect of the antisolvent and gas

quenching causes instant supersaturation of precursor solution and grants fast nucleation and rapid removal of solvents, promoting the homogeneity of PVSK film in the whole substrate.<sup>56</sup> Moreover, gas quenching of PVSK deposition and antisolvent quenching was set at a lower flow with respect to the mini-module (see Section 4) to prevent defects formation due to local high-rate evaporation spots and unwanted early conversion of PVSK before the antisolvent quenching. The module efficiency was 12.58% with improved current ( $I_{sc}$  = 218.06 mA,  $J_{sc}$  = 18.75 mA/cm<sup>2</sup>) and voltage (17.68 V, 1.11 V per cell) (Figure 2B). We compared the PVSK film absorbance spectra of the initial and final parts of both blade-coated and hybrid meniscus-coated modules (Figure 3A).

In the latter case, the curves are quite similar, showing a good uniformity of the PVSK deposition on the entire area, unlike the blade-coated case. In the blade-coated substrate, the final part of the coated substrate has a low absorbance spectrum due to a reduction of the PVSK amount compared to the initial part. The absorbance spectra for the hybrid meniscus-coated module is relatively higher than the bladed meniscus-coated one, which can be attributed to the larger grain size from SEM images (Figure 4A,B).

We pursued two strategies to boost performance and get superior quality of such large-area devices. The first one is related to the surface defects passivation of the PVSK layer and the second one is related to the PVSK additive engineering to improve nucleation and quality of the absorber material.

The losses caused by layers' inhomogeneity are related to the difficulties in transferring to sub-module devices deposition processes and material compositions optimized for mini-modules obtained with scalable or unscalable techniques.<sup>12</sup> In this context, the polycrystalline nature of solution-processed PVSK layers induces defects, such as at grain boundaries and vacancies during the fabrication process.<sup>13</sup> Moreover, many defects trap states can occur.<sup>57–59</sup> Since in any kind

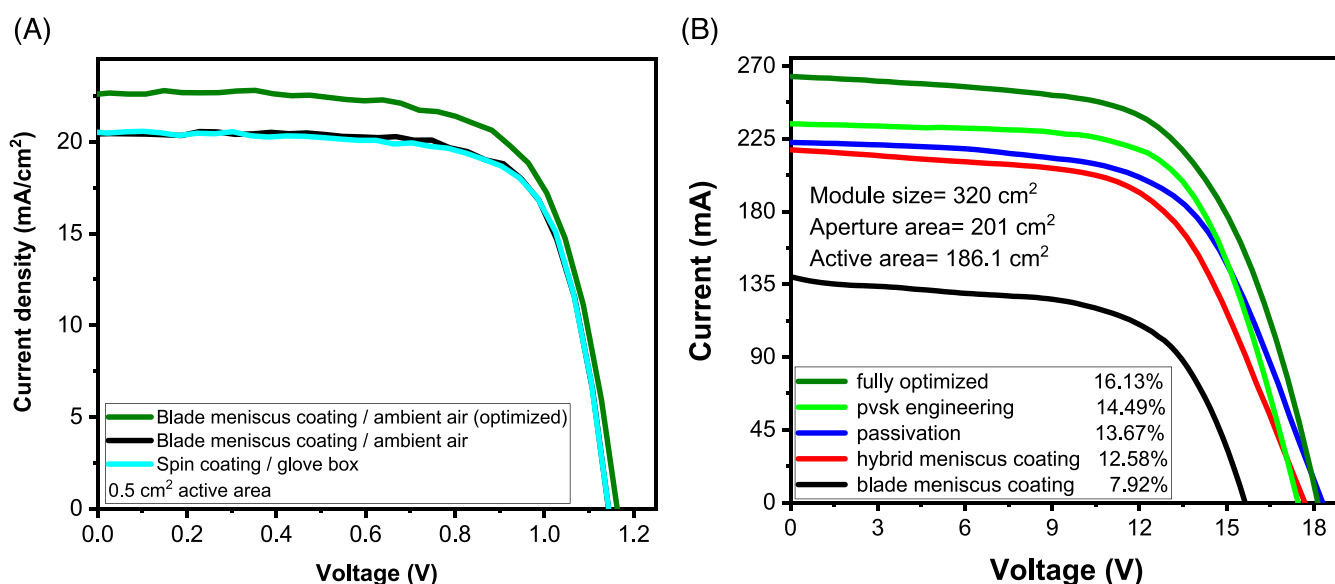


**FIGURE 2** (A) Cell (0.5 cm<sup>2</sup> active area) current density/voltage plot. (B) Sub-modules current/voltage curves according to the different optimization steps. [Colour figure can be viewed at [wileyonlinelibrary.com](http://wileyonlinelibrary.com)]

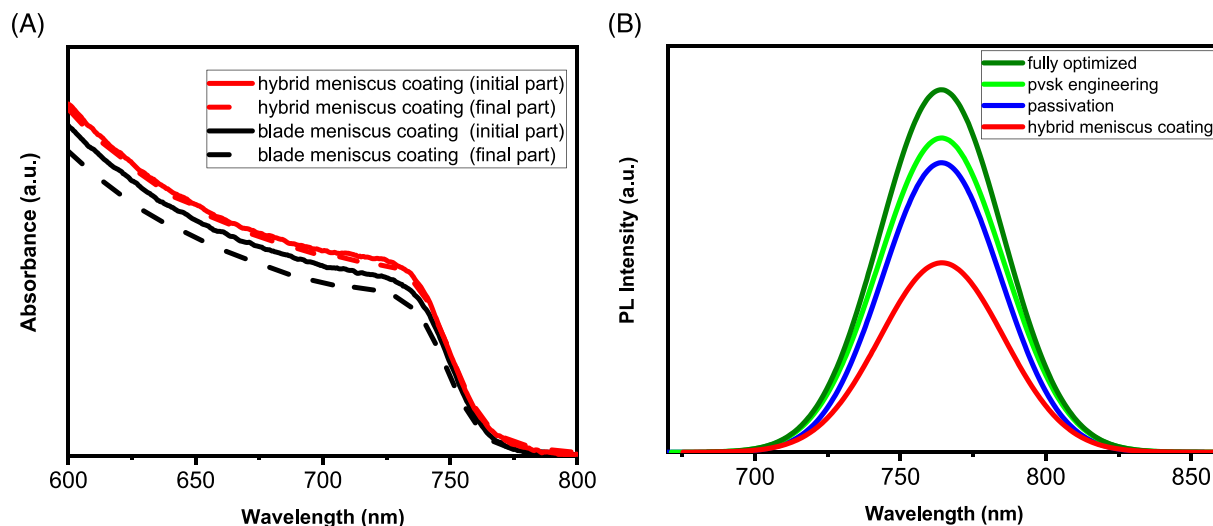


**FIGURE 3** (A) UltraViolet-Visible (UV-Vis) absorption spectra at the beginning and at the end part of the deposition. (B) Photoluminescence (PL) of perovskite (PVSK) layer related to the optimization method. [Colour figure can be viewed at [wileyonlinelibrary.com](http://wileyonlinelibrary.com)]

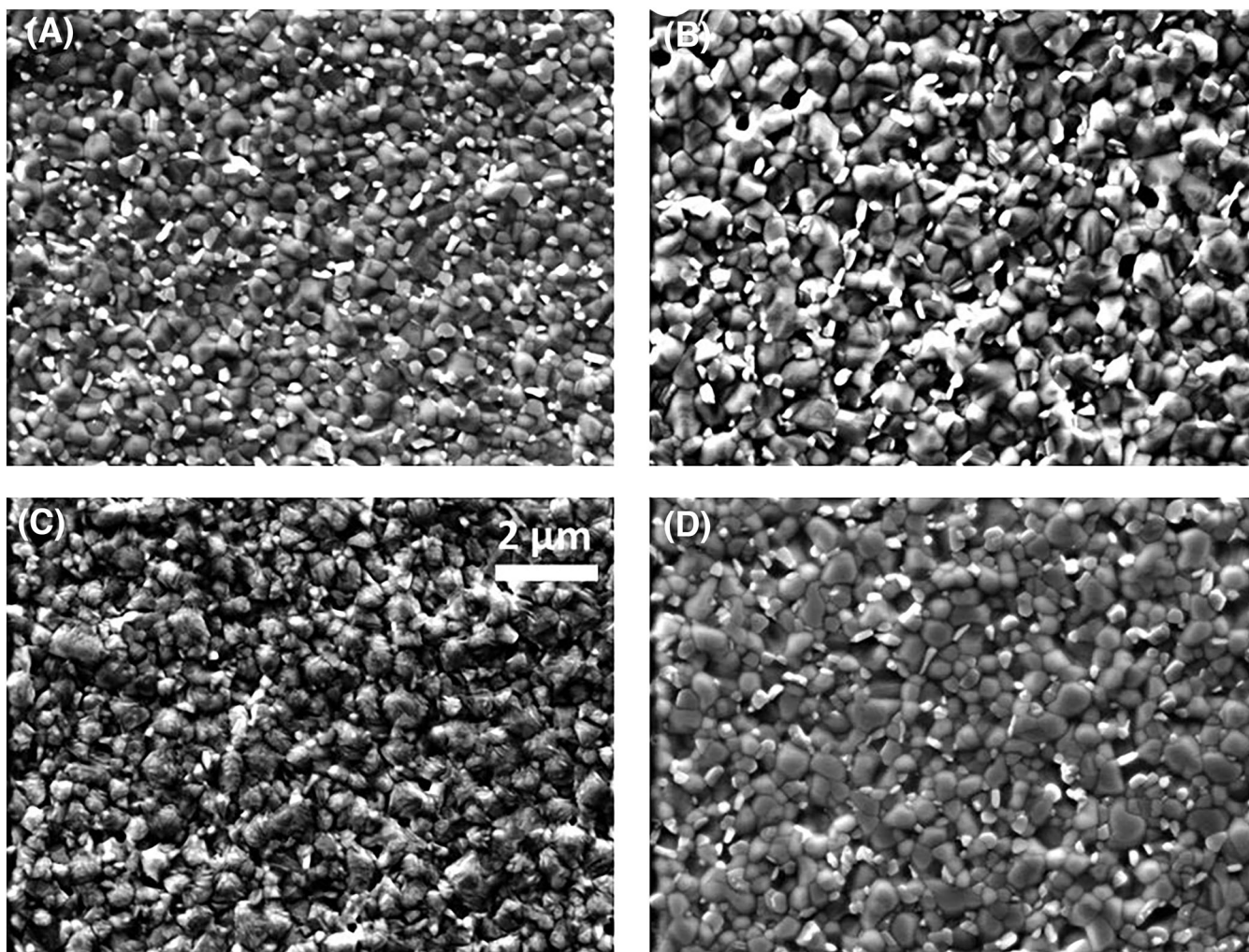


**FIGURE 4** Perovskite (PVSK) top view SEM images: (A) blade-coating deposition; (B) hybrid meniscus coating; (C) phenethylammonium iodide (PEAI) passivating agent on top of the PVSK layer; (D) hybrid meniscus coating of PVSK compound with acetonitrile (ACN) solvent addition.

of solar cell defects are mainly localized at the surface/interface,<sup>60,61</sup> the PVSK surface passivation by phenethylammonium iodide (PEAI) is one of the most efficient methods to suppress nonradiative recombination losses and to improve charge carrier extraction and photovoltage, by forming a shielding layer in such a way more effective than 2D PEA<sub>2</sub>PbI<sub>4</sub> PVSK.<sup>58,59,62–64</sup> In a recent work, we adopted PEA<sub>2</sub>PbI<sub>4</sub> as surface passivation material on mini-module size to suppress PVSK defects.<sup>11</sup> The passivation agent was deposited in the glove box by spin coating technique, here, we transfer this process in ambient air by slot-die coating technique and gas quenching to dry the excess of IPA. We performed X-ray diffraction (XRD) on PVSK films with and without the PEA<sub>2</sub>PbI<sub>4</sub> passivation agent to prove the presence of the PEA<sub>2</sub>PbI<sub>4</sub> on the 3D PVSK surface (Figure S3). In both cases, the XRD pattern shows a peak at 12.7° related to the PbI<sub>2</sub> excess in the crystalline 3D PVSK film.<sup>64</sup> A new diffraction peak appeared at about 4.7° in the case of PVSK with PEA<sub>2</sub>PbI<sub>4</sub> that is related to the PEA<sub>2</sub>PbI<sub>4</sub> crystal itself.<sup>11,63</sup> The beneficial effect of the passivation layer is proved by the steady photoluminescence (PL) intensity increasing in the case of the PEA<sub>2</sub>PbI<sub>4</sub> passivating agent (Figure 3B). The reason behind this PL enhancement is related to the decrease of the recombination in the PVSK layer,<sup>59,65</sup> since PEA<sub>2</sub>PbI<sub>4</sub> treatment suppresses the surface nonradiative recombination defects.<sup>63</sup> The SEM image in Figure 4C reveals the PEA<sub>2</sub>PbI<sub>4</sub> layer covering the PVSK surface. The roughness measured by the profilometer is about 35 and 22 nm without and with the PEA<sub>2</sub>PbI<sub>4</sub> layer, respectively, because the passivating agent is deposited easily at the grain boundary reducing the height difference between the grain surface and the boundary.<sup>63</sup> The module efficiency improved to 13.67% (I<sub>sc</sub> = 222.48 mA, V<sub>oc</sub> = 18.3 V, FF = 62.46%) and, as expected, the most affected parameter was the V<sub>oc</sub> (Figure 2B) because the recombination has largely been suppressed in the PVSK layer.<sup>11,63</sup>

Besides the surface passivation, we engineered the PVSK precursor solution with a solvent additive to control the intermediate phase of the PVSK wet film and get superior crystal quality reducing defects and controlling the nuclei formation. The solvent is a medium to dissolve the PVSK precursors and its features (e.g., boiling point, viscosity, vapor pressure, polarity, and coordination ability) are directly linked to the film-forming process regardless of the adopted coating technique.<sup>66</sup> In literature, solvent additives are deeply studied to overcome different issues related to deposition quality and PVSK compositions. A cyclic-urea (1,3-dimethyl-2-imidazolidinone, DMI),  $\gamma$ -butyrolactone (GBL), or a mixture of MA:ACN (methylamine, acetonitrile) are employed in spin coating technique to get repeatable and fast crystallization of MAPbI<sub>3</sub> PVSK.<sup>66–69</sup> In the case of PVSK solutions for ambient air coating techniques, high vapor pressure solvents are generally preferred to fast dry DMF:DMSO mixture. Chen et al. demonstrated how DMSO was trapped during film formation forming voids at the PVSK-substrate interface and causing PVSK film degradation.<sup>23</sup> Different solvent additives such as ethanol, tetrahydrothiophene1,1-dioxide (sulfolane), and a mixture of 2-methoxyethanol, acetonitrile, and dimethyl sulfoxide (2-ME):ACN:DMSO aim to control morphology and crystallinity of PVSK layer and to increase repeatability and feasibility of the

deposition process.<sup>66,70,71</sup> Concerning this, our strategy is focused on adding high vapor pressure non-coordinating ACN solvent in PVSK solution that can uniform the evaporation rate and the supersaturated phase of the absorber film on large substrate area. We got an efficiency of 14.49% (V<sub>oc</sub> = 17.45 V, FF = 66%) with improved current I<sub>sc</sub> = 234.11 mA (J<sub>sc</sub> = 20.13 mA/cm<sup>2</sup>) (Figure 2B). The enhancement is ascribed to reduced nonradiative recombination channel in the PVSK film due to less grain boundaries and thus trap states, as shown by higher PL intensity in the case of PVSK film with ACN addition (Figure 3B).<sup>72</sup> This is confirmed by SEM images (Figure 4D) showing larger grains and less holes when ACN solvent is added to the PVSK compound.

The advantages related to the passivation and solvent addition strategies (i.e., higher voltage and current) led to a champion efficiency of 16.13% (15% on aperture area) with V<sub>oc</sub> = 18.15 V, I<sub>sc</sub> = 263.42 mA, J<sub>sc</sub> = 22.65 mA/cm<sup>2</sup>, and FF = 62.8% (Figure 2B). The performance is comparable to that obtained with the mini-module reported in our recent work.<sup>5</sup> Moreover, the reduction of PCE is less than 10% with respect to 0.5 cm<sup>2</sup> blade-coated cells (champion PCE = 17.91%, 3% standard deviation) fabricated by adopting the PEA<sub>2</sub>PbI<sub>4</sub> passivation and the PVSK engineering (Figures 2A, S1). The stabilized efficiency at 1 SUN MPP is 15.5% (Figure 5A).<sup>73</sup>

Electroluminescence (EL) advanced module characterization allows us to realize a deep failure analysis. EL on module devices can be helpful in detecting degraded, cracked cells or failed connections and is very sensitive to non-selective interfaces and inhomogeneities in the functional layers.<sup>5,74</sup> In Figure 5B, EL (20 V injection voltage) shows small defects and local variation of series resistance because of some indiscernible inhomogeneities in the crystal growth that do not reflect a huge thickness variation, as reported in our recent work.<sup>5</sup> Furthermore, the high EL intensity reveals the homogeneity and the interface quality of the meniscus-coated PVSK layer without any shunt defects. Moreover, EL contributions are not present outside the aperture area. PVSK SEM images gathered from three different locations (Figure S4) on the sub-module area exhibited a high level of uniformity. The high-quality PVSK bladed films and large-scale uniformity are obtained thanks to the control of the crystallization process according to the LaMer mechanism.<sup>75</sup> The supersaturation phase is obtained when PVSK solution is coated onto the substrate and the dry-air knife permits the rapid evaporation of DMF:DMSO mixture, yielding a high rate of crystal nucleation on the whole substrate uniformly.<sup>76</sup> After this, the antisolvent realizes the “burst nucleation,” extracting suddenly the large amount of the solvent stacked in the film, increasing suddenly the concentration of the monomers over the supersaturation limit and starting the growth of crystals by diffusion. Finally, the dry-air knife removes all the solvents, enhancing the growth rate and preventing solvent from sticking onto the PVSK, with a shine and low-defect film feature.

The stability of the encapsulated sub-module was tested according to ISOS-D-1 (RT and ambient humidity) at V<sub>oc</sub> for more than 3000 h (Figure 5C).<sup>77</sup> After 100 h, the sub-module lost less than 4% PCE, and at 3200 h, the decreasing efficiency was less than 10% (as after 1000 h) but still above the T<sub>80</sub>.<sup>78</sup>

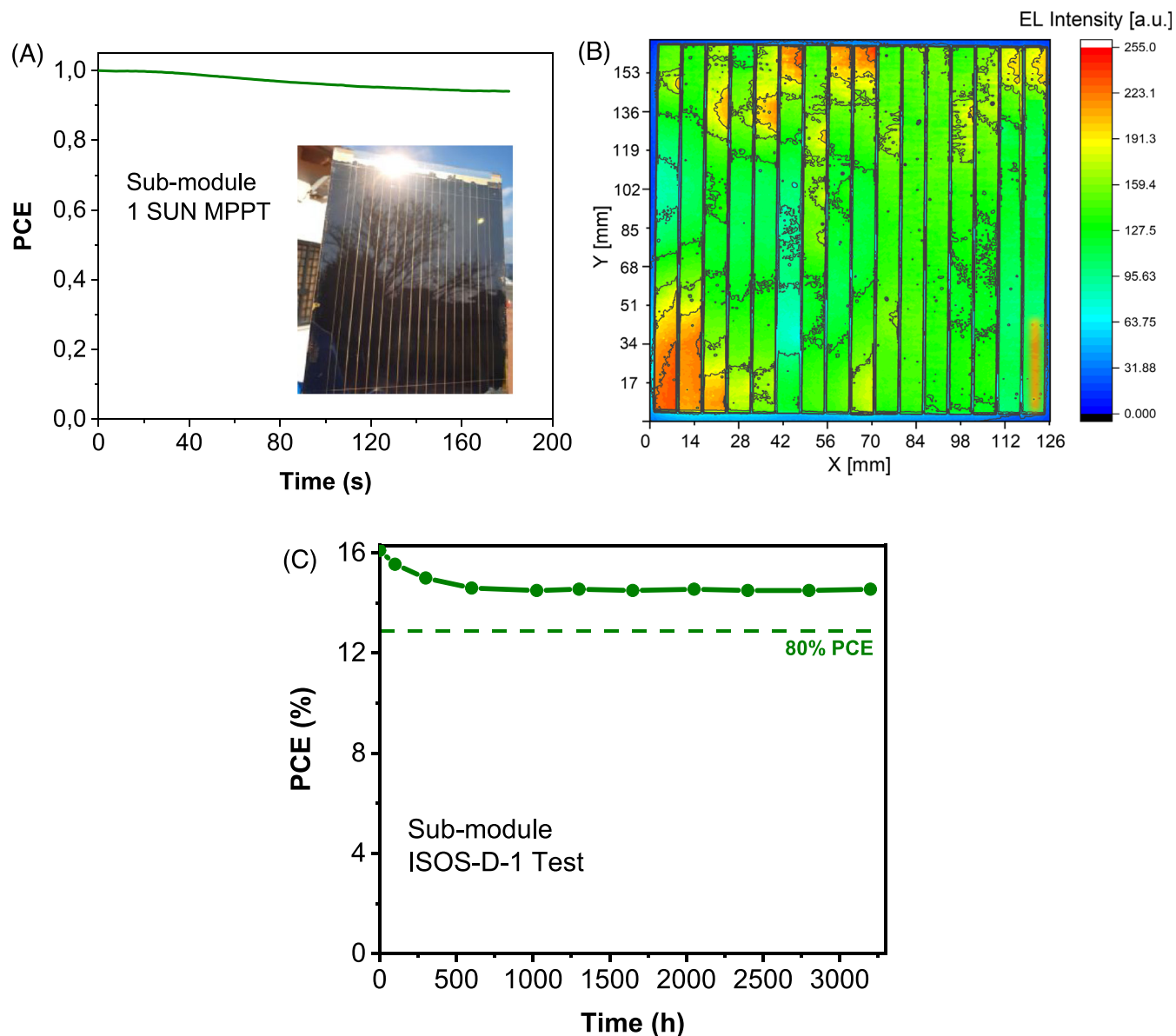


**FIGURE 5** (A) Maximum power point (MPP) at 1 SUN, (B) electroluminescence (EL) imaging and (C) ISOS-D-1 stability test of the fabricated perovskite (PVSK) sub-module. [Colour figure can be viewed at [wileyonlinelibrary.com](https://onlinelibrary.wiley.com/doi/10.1002/prop.3741)]

## 2.2 | Laser patterning and module layout

The module design and the interconnection patterning can face and limit losses induced by front contact and cell interconnections.<sup>5,79</sup> In the upscale process the P2-P3 ablation steps by a laser source (here Nd:YVO<sub>4</sub>) are crucial to obtain low losses. The P2 (Section 4) removes the full stack (ETL/PVSK/PEAI/HTL) deposited on FTO from the vertical connection areas to series connect two adjacent cells by the metal counter-electrode. In our recent paper, we reported the optimization procedure to optimize fluence and raster scanning distance (RSD), therefore obtaining a full stack removal (i.e., etching depth comparable to the full stack thickness) by avoiding the TCO damaging and limiting the contact resistance between gold/TCO.<sup>11</sup> Here, the sheet resistance in the P2 trench is equal to 7  $\Omega/\square$  as the bare FTO. Moreover,

we report the top-view energy-dispersive X-ray spectroscopy (EDX) elemental analysis of the P2 ablation to testify to the full stack removal (Figure S5). The images showed that Pb, I, C, and Br (i.e., the PVSK forming elements) have been reduced in the P2 area with respect to the area surrounding it, while the FTO integrity is testified by the Sn strong signal. In the same image, about 600  $\mu\text{m}$  dead area width is reported. This leads to an aperture area of 201  $\text{cm}^2$  and a GFF equal to 93%.

## 2.3 | Life cycle analysis

This section is focused on the results of the LCA that includes an economic and environmental assessment based on primary data, gathered

during the manufacturing of the PVSK devices at different scales. In Figure 6, charts highlight the environmental impact assessment results of the PVSK mini- and sub-module described in the previous sections. Consistently with the aim of the analysis, which is to evaluate the economic and environmental effects of the scaling up, results are provided as a relative comparison between the two devices. A more detailed overview of all the environmental impact values is provided in the [Supporting Information](#).

The histograms illustrated in Figure 6A show the outcomes concerning the characterization of the environmental impacts of the mini-module fabrication, by focusing on the percentage contribution of each process step to the overall eco-profile of the manufacturing chain.

By observing the stacked columns depicted in Figure 6A, it is possible to remark that gold evaporation is overall the main contributor to all the midpoint impact categories. This outcome is related both to the energy required by this process step, which strongly affects some indicators like “climate change,” and to the materials consumption, especially when considering the category “resource use, minerals, and metals.” However, the realization of the TiO<sub>2</sub> layer—which includes a compact layer deposition, the blading, and the sintering of the material—is also responsible for a significant contribution to the overall environmental burdens. Indeed, such manufacturing steps are very energy intensive as they include high-temperature processes. Another impacting contribution to the eco-profile of the mini-module is given by the FTO-glass layer, especially for the “human health, non-cancer” category, and the cleaning stage; on the other hand, the contribution of the other processes is almost negligible as it is overall assessed below 5%.

Figure 6B shows the outcomes concerning the characterization of the environmental impacts of the sub-module considering the same environmental indicators adopted for the mini-module. As detailed in the life cycle inventory (LCI) analysis section available in Tables S1 and S2, the mini-module upscale requires the implementation of some changes in the construction materials. For instance, the processes related to the TiO<sub>2</sub> layer (compact layer deposition, sintering, and blading) are replaced with the tin-oxide deposition and firing steps. Moreover, a PEAL layer is also added to the module architecture as well as ACN PVSK solvent additive. The main evidence that can be observed from the inspection of Figure 6B is that, compared to the environmental characterization of the mini-module, in which the manufacturing steps related to the TiO<sub>2</sub> layer represent a major contribution, the percentage impact of the tin oxide is much lower. Similarly, the other additional materials that are employed to scale up the size of the device, such as the PEAL and the ACN, provide a negligible contribution. Indeed, as highlighted in Figure 6B, the FTO-glass and the gold evaporation processes are the only steps that provide remarkable environmental burdens, whereas the other processes have a percentage impact that is equal at most to 10%.

Figure 6C shows the comparison between the environmental impacts of the mini- and the sub-module, analyzing all the indicators proposed by the calculation method EF 3.0.<sup>80</sup> This chart highlights

that the scale-up operation allows for strong impact mitigation in all the environmental categories. According to the considerations related to the analysis of Figure 6A,B, the reduction is strictly correlated to the replacement of the TiO<sub>2</sub> with tin-oxide. Indeed, when analyzing the mini-module's impacts, for which the TiO<sub>2</sub> layer represents the main contributor (such as “climate change,” “resource depletion, fossil,” and other indicators), we observe a very strong reduction of the environmental load; for these categories, the benefits can be up to −65%. On the other hand, when analyzing the indicators “human toxicity, non-cancer” and “resource use, minerals, and metals,” for which the TiO<sub>2</sub> layer of the mini-module is less impactful, lower impact mitigation can be observed, namely, −37% and −21%, respectively. More in general, the scale-up operation for mini- to sub-modules allows for more efficient consumption of the resources, whether we consider materials or energy. Hence, all the processes result in being more sustainable in the sub-module than in the mini-modules (see Tables S3–S5).

The LCA presented in this paper also includes the calculation of the manufacturing costs (Figure 7).

Such economic assessment accounts for three cost items, namely, the cost of the mini- and sub-module materials, the cost of the energy consumed by the production line, and the cost of the equipment, depreciated in a time range of 10 years.<sup>50</sup> The costs related to human labor and the maintenance of the production line are not included as they are not relevant for the comparison of the modules; moreover, they are affected by a strong uncertainty as the manufacturing is carried out at the laboratory level. Figure 7A demonstrates that over the large environmental benefits of the scale-up, moving from the mini- to the sub-module also allows for a strong reduction of the manufacturing costs from 0.086 €/cm<sup>2</sup> to 0.034 €/cm<sup>2</sup>. This outcome results from enhanced resource management when scaling up the production of the device. More specifically, as underlined in Figure 7B, most of the expenses are related to the materials. Particularly, the consumption of lead iodide and lead bromide during the PVSK deposition as well as the consumption of Spiro-OMeTAD, which is the most expensive material, represent together 67% of the expenses for the raw materials of the mini-module (0.038 €/cm<sup>2</sup>). On the other hand, when analyzing the sub-module, the same above-mentioned materials result as the most expensive, but their specific cost is remarkably reduced compared to the mini-module (0.012 €/cm<sup>2</sup>). However, when operating with larger areas, the equipment can produce a larger throughput with fewer energy inputs per square centimeter. Therefore, the costs for electricity and equipment depreciation are also mitigated during the scale-up, and their percentage contribution to the total manufacturing cost of the sub-module is slightly varied compared to the mini-module.

Focusing on the adoption of the antisolvent in the scale-up operations, and more specifically on the PVSK deposition, it is possible to observe that the environmental burdens of this material are negligible compared to the impacts of the overall device. Indeed, depending on the selected environmental indicator, the percentage contribution of the antisolvent to the overall eco-profile of the sub-module ranges between 0.0007% and 0.0536%. On the other hand, although its



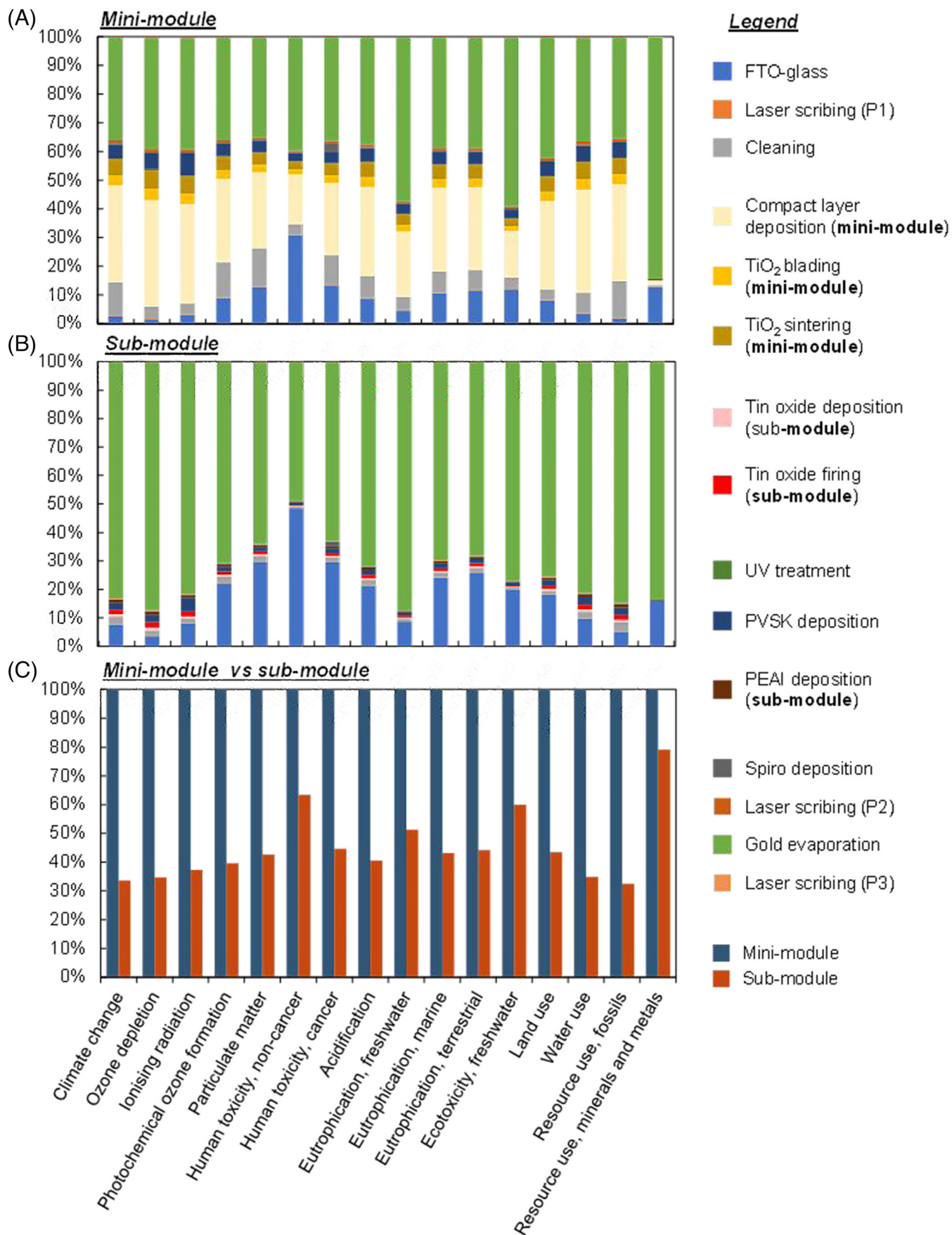


**FIGURE 6** Midpoint environmental impact characterization of (A) the mini-module and (B) of the sub-module; (C) comparison between the eco-profiles of the mini- and the sub-module. [Colour figure can be viewed at [wileyonlinelibrary.com](http://wileyonlinelibrary.com)]

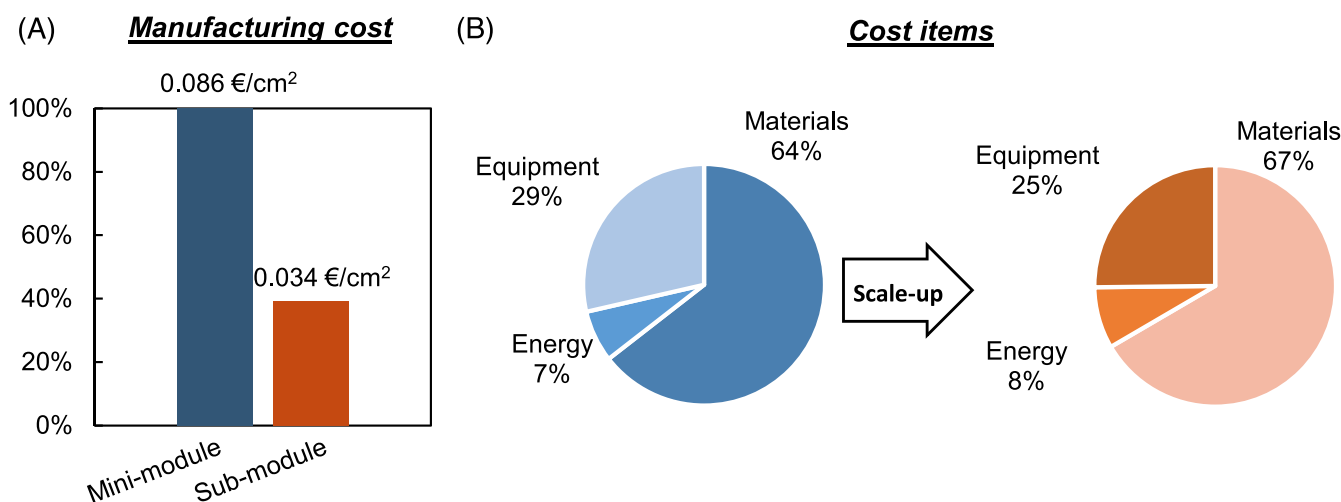


**FIGURE 7** Comparisons between the (A) manufacturing costs of mini- and sub-module and (B) cost items (materials, energy, and equipment). [Colour figure can be viewed at [wileyonlinelibrary.com](http://wileyonlinelibrary.com)]

relatively high market price (120 €/l), the consumption of antisolvent represents 0.02% of the manufacturing cost of the sub-module due to the low quantity of this material employed in the process. Hence, based on these results, it is possible to remark that adding the antisolvent to the sub-module's process flow does not represent a critical issue for the economic and environmental sustainability of the scale-up operation.

### 3 | CONCLUSION

The uniform deposition of PVSK and transporting layers on large-area devices is one of the most challenging aspects of module fabrication.<sup>5,35,81</sup> In the last years, PVSK mini-modules and sub-modules reached efficiencies of about 10% and 35% less compared to small area cells, respectively. The losses are related to the front contact sheet resistance, and the interconnection dead-area and resistance. When scaling to sub-module size, layer inhomogeneity losses have a huge impact on device performance and are mainly related to the coating technique, the material composition, and the deposition environment. The target is to realize optimized scalable processes to minimize losses and to reduce materials waste. We demonstrated a planar PVSK sub-module (201 cm<sup>2</sup> aperture area, 93% GFF) fully fabricated outside the glovebox (first time in literature) by meniscus coating techniques in real manufacturing conditions. We adopted the passivation strategy to suppress nonradiative recombination losses and to improve charge carrier extraction and photovoltage. Moreover, we engineered the PVSK precursor solution with ACN to control the intermediate phase of the absorber film. The materials, device and process optimizations lead to an efficiency of 16.13% (93% GFF) with 7% losses with respect to 0.5 cm<sup>2</sup> cell and no losses with respect to the mini-module.<sup>5</sup> Different characterization techniques (SEM, PL, and UV-Vis) testified the homogeneity of the deposited layers on the full device area. EL reveals the homogeneity and the interface quality

of the meniscus-coated PVSK layer without any shunt defects. The sub-module has a stabilized efficiency of 15.5% and is stable for more than 3000 h according to ISOS-D-1. The LCA demonstrated the economic and environmental advantages deriving from the materials and the process adopted. Finally, the reported sub-module showed outstanding efficiency, stability, sustainability, and low cost.

## 4 | EXPERIMENTAL SECTION

### 4.1 | Small area cells (0.5 cm<sup>2</sup>) fabrication

#### 4.1.1 | Blade coating process

FTO-glass substrate (5 cm<sup>2</sup> × 7.5 cm<sup>2</sup>) were patterned with two longitudinal scribes (P1) by a nanosecond raster scanning laser ( $\lambda = 355$  nm, Nd:YVO<sub>4</sub> pulsed at 80 kHz, fluence = 10.2 J/cm<sup>2</sup>). The substrates were cleaned with soap/water solution and then sonicated in acetone, ethanol, and 2-propanol for 10 min each, respectively. After sonication, the samples were transferred to a UV-Ozone lamp for 30 min to eliminate the organic residual. Before tin oxide deposition, each substrate was treated for 10 min in a UV-Ozone lamp to improve the wettability of the aqueous solution. A total of 70  $\mu$ L of SnO<sub>2</sub> solution (1:7 v/v in water, from Alfa Aesar Colloidal dispersion 15% in water, stirred, sonicated, and filtered) were blade-coated at 80°C with blade height and speed of 100  $\mu$ m and 15 mm/s, respectively. After deposition, the substrates were annealed at 150°C in air for 30 min. 3C PVSK (Cs<sub>0.05</sub>(MA<sub>0.17</sub>FA<sub>0.83</sub>)<sub>0.95</sub>Pb(I<sub>0.83</sub>Br<sub>0.17</sub>)<sub>3</sub> in DMF/DMSO (Lead iodide from TCI Co. Ltd; CsI, FAI and MABr from Great Cell Solar) was deposited by blade coating (ambient air, 30% RH) technique according to Vesce et al.<sup>5</sup> The blade coating deposition process was assisted by a controlled and heated (40°C) airflow to pre-dry the PVSK surface. The antisolvent washing (IPA from Sigma-Aldrich) is performed by the same deposition method with blade

height and speed of 300  $\mu\text{m}$  and 20 mm/s, respectively. Air blade knife at 220 L/min helped the conversion of PVSK as discussed in the manuscript and here.<sup>5</sup> Finally, the substrates were annealed at 100°C on a hot plate for 1 h. Regarding the ACN-modified PVSK, the molarity of the solution was maintained equal to the prior one. ACN was added as 20% of the final volume in the DMF/DMSO 4:1 mixture. About the passivation layer, we transferred to the out-of-glove-box blade coating technique the process showed recently and adopted for the spin-coated cells.<sup>11</sup> Phenethyl ammonium iodide (Dyename) solution 5 mM in IPA was blade coated (300  $\mu\text{m}$  gap, speed 20 mm/s) on top of PVSK assisted by dry-air quenching at RT and 140 L/min flow. HTM Spiro-OMeTAD solution (95 mg/mL in chlorobenzene) doped with 20  $\mu\text{L}$  of lithium bis(trifluoromethanesulfonyl)imide solution (520 mg/mL in ACN) and 35  $\mu\text{L}$  of 4-tert-butylpyridine was blade-coated on PVSK layer. The height of the blade is fixed at 200  $\mu\text{m}$  and the blade speed at 20 mm/s. The process was assisted by air blowing (140 L/min) at room temperature to fast dry chlorobenzene solvent and obtain a uniform layer (see manuscript and here<sup>5</sup>). Once HTM is deposited, the 5 cm<sup>2</sup>  $\times$  7.5 cm<sup>2</sup> substrates were cut into six devices (2.5 cm<sup>2</sup>  $\times$  2.5 cm<sup>2</sup> each) and then 100 nm of gold was thermally evaporated as the top electrode.

#### 4.1.2 | Spin coating process

FTO-glass substrate (2.5 cm<sup>2</sup>  $\times$  2.5 cm<sup>2</sup>) were patterned with two longitudinal scribes (P1) by a nanosecond raster scanning laser ( $\lambda = 355$  nm, Nd:YVO<sub>4</sub> pulsed at 80 kHz, fluence = 10.2 J/cm<sup>2</sup>). The substrates were cleaned with soap/water solution and then sonicated in acetone, ethanol, and 2-propanol for 10 min each, respectively. After sonication, the samples were transferred to a UV-Ozone lamp for 30 min to eliminate the organic residual. Before tin oxide deposition, each substrate was treated for 10 min in a UV-Ozone lamp to improve the wettability of the aqueous solution. A SnO<sub>2</sub> solution in water (Alfa Aesar, 1:7 v/v) is stirred, sonicated, and filtered prior to the deposition step. The as-prepared solution is spin-coated (2800 rpm, 2 s ramp up, 60 s) onto the substrates and then annealed on a hot plate at 150°C for 10 min in ambient air. The triple cation PVSK (Cs<sub>0.05</sub>(MA<sub>0.17</sub>FA<sub>0.83</sub>)<sub>0.95</sub>Pb(I<sub>0.83</sub>Br<sub>0.17</sub>)<sub>3</sub> in DMF/DMSO, 1.42 M) (Lead Iodide from TCI Co. Ltd; CsI, FAI, and MABr from Great Cell Solar) is deposited by spin coating technique in N<sub>2</sub> filled glove box environment. The precursor solution and, secondly, chlorobenzene are spun onto the substrate. The spin-coating parameters are 1000 rpm, 5 s ramp up, 10 s then 5000 rpm, 2 s ramp up, 30 s. Then, we add chlorobenzene 7 s before ending for both small and large area devices. After spin coating, the PVSK is annealed at 100°C for 60 min. Dyename PEAI passivation material in IPA (3.74 mg/mL) and HTL Spiro-OMeTAD solution in chlorobenzene (95.1 mg/mL) doped with TBP (35.5  $\mu\text{L}$ ) and Li-TFSI (20.6  $\mu\text{L}$  from a stock solution of 520 mg/mL) are spin-coated (PEAI at 2000 rpm, 0 s ramp up, 25 s; Spiro at 4000 rpm, 2 s ramp up, 20 s) on top of the PVSK layer subsequently. After that, 100 nm thick gold counter-electrode is thermally evaporated.

## 4.2 | Sub-module fabrication

### 4.2.1 | Substrate preparation

FTO-glass substrates (7  $\Omega/\text{sq}$ , Pilkington) were patterned (P1) to form 16 series connected cells by a nanosecond raster scanning laser ( $\lambda = 355$  nm, Nd:YVO<sub>4</sub> pulsed at 80 kHz, fluence = 10.2 J/cm<sup>2</sup>). The substrates are cleaned with a soap/water solution and then with acetone, ethanol, and 2-propanol. After solvent washing, the samples were transferred in a UV-Ozone lamp for 30 min to eliminate the organic residual.

### 4.2.2 | ETL

Before tin oxide deposition, each substrate was treated for 10 min in UV-Ozone lamp to improve the wettability of the aqueous solution, then a colloidal solution of tin oxide diluted in water 1:7 v/v (from 15% colloidal solution Alfa Aesar, stirred, sonicated, and filtered) was deposited on top of pre-heated substrate at 80°C by slot-die coating technique. The rate flow and the distance between the slot-die head and substrate were 2000  $\mu\text{L}/\text{min}$  and 100  $\mu\text{m}$ , respectively. The blade speed was 15 mm/s. Then the film was annealed in air at 150°C for 30 min to obtain about 40 nm thick SnO<sub>2</sub>.

### 4.2.3 | PVSK layer

The substrates were treated under a UV-oven ozone lamp to improve the wettability prior to the PVSK deposition. The 3C PVSK 1.1 M solution (Cs<sub>0.05</sub>(MA<sub>0.17</sub>FA<sub>0.83</sub>)<sub>0.95</sub>Pb(I<sub>0.83</sub>Br<sub>0.17</sub>)<sub>3</sub> in DMF/DMSO) (Lead Iodide from TCI Co. Ltd; CsI, FAI, and MABr from Great Cell Solar) was deposited by hybrid blade/slot-die coating (ambient air, 30% RH) technique on a thermal plate at 40°C. The blade coating deposition process of the PVSK precursor was assisted by a heated (40°C) airflow (220 L/min) to pre-dry the PVSK surface. The gap between substrate and blade was 500  $\mu\text{m}$  and the speed of the plate was fixed at 10 mm/s. After the pre-drying step, antisolvent deposition was carried out by slot-die coating isopropanol with a speed of 20 mm/s, flow rate of 4000  $\mu\text{L}/\text{min}$ , slot-die head at 300  $\mu\text{m}$ , and 40°C airflow at 220 L/min. Finally, the substrates are annealed at 100°C on a hot plate for 20 min.

Regarding the ACN-modified PVSK, the molarity of the solution was maintained equal to the prior one. ACN was added as 20% of the final volume in the DMF/DMSO 4:1 mixture. The deposition parameters for blade and slot-die coating steps were not changed apart for the lower airflow in both cases fixed at 180 L/min to avoid early PVSK conversion and DMSO trapping during the first step.

### 4.2.4 | PEAI passivation

Here, we transferred to the out-of-glove-box slot-die coating technique the process showed recently and adopted for the spin-coated

cells.<sup>11</sup> Phenethyl ammonium iodide (Dyename) solution 5 mM in IPA was slot-die coated (2000  $\mu\text{L}/\text{min}$  rate, 300  $\mu\text{m}$  gap, speed 20 mm/s) on top of PVSK assisted by dry-air quenching at RT and 140 L/min flow.

#### 4.2.5 | HTL and top-electrode

The HTM Spiro-OMeTAD solution (60 mM, Sigma Aldrich) in chlorobenzene (the molar ratio between the dopants and the Spiro-OMeTAD is 0.5, 3.3 for lithium bis(trifluoromethanesulfonyl)imide and 4-tert-butylpyridine, respectively) was coated by an air-assisted slot-die method in ambient. The gap between slot-die head and substrate was 200  $\mu\text{m}$ , the speed 20 mm/s, the airflow 145 L/min, and the slot-die rate flow 2000  $\mu\text{L}/\text{min}$ . The next step is the removal (P2) of the full stack (ETL/PVSK/PEAI/HTL) deposited on FTO from the vertical connection areas to series connect two adjacent cells with the subsequent electrode deposition. Substrates were transferred on a raster scanning laser for the P2 process ( $\lambda = 355$  nm, Nd:YVO<sub>4</sub> pulsed at 80 kHz, fluence = 213  $\text{mJ cm}^{-2}$ ). Afterwards, 120 nm thick Au counter-electrode is thermally evaporated in a high vacuum chamber ( $10^{-6}$  mbar). Finally, the counter electrode P3 ablation is performed ( $\lambda = 355$  nm, Nd:YVO<sub>4</sub> pulsed at 80 kHz, fluence = 200  $\text{mJ cm}^{-2}$ ) to obtain the electrical insulation between the counter electrodes of adjacent cells. The patterned module shows 16 series connected cells with 11.63  $\text{cm}^2$  cell area, about 600  $\mu\text{m}$  dead area width, a total active area of 186.1  $\text{cm}^2$ , an aperture area of 201  $\text{cm}^2$ , and a GFF equal to 93%.

#### 4.2.6 | Sealing

The device was sealed by dispensing a UV-curable resin on the module's perimeter prior to placing a second top glass (2 mm thick). During this process, no O<sub>2</sub> was left between the two glasses after sealing.<sup>5</sup>

#### 4.2.7 | Device characterization

The PV characteristics and the MPP tracking are measured with a class A sun simulator (Sun 2000, Abet) at AM 1.51000  $\text{W}/\text{m}^2$  calibrated with an SKS 1110 sensor (Skye Instruments Ltd., Llandrindod Wells, UK); the system is equipped with a 2612 source meter (Keithley Instruments Inc., Cleveland, OH, USA) and a LabVIEW interface. A LabVIEW/Python-based code manages the JV and MPP tracking state. A standard perturb and observe tracking algorithm is selected for the devices.<sup>73</sup> The optical analysis is performed with a UV-Vis spectrometer (UV-2550, Shimadzu) and with a PL measurement system (Arceo, Cicci Research). SEM images are acquired by the VEGA 4 TESCAN Analytics machine at 15 keV. XRD measurements are carried out using a Rigaku Smartlab SE. The film roughness is measured using a profilometer (DEKTA 150, Veeco Instruments Inc.). The EL imaging on the module adopts a Silicon

CCD camera. The illumination intensity was kept constant for the different measurements.

### 4.3 | Life cycle analysis

According to the ISO 14040 Family Standards and Guidelines,<sup>82,83</sup> and the more completely elaborated ILCD Handbook Guidelines,<sup>84</sup> an attributional cradle-to-gate approach was implemented for the environmental LCA calculation of the hybrid blade/slot-die coating method. The functional unit chosen in this study is the 1  $\text{cm}^2$  area of the manufactured module. No allocation procedure nor system expansion approach was required since all the environmental burdens were attributed to the final product of the process. Data LCI was built based on lab primary data and system boundaries are defined so that the foreground system is focused on the manufacturing procedure. When needed, meta-data (conveniently customized to generate datasets for input materials) and secondary data were taken from the Ecoinvent Database v. 3.7.1.<sup>85</sup> Equipment and instruments are not included in the system modeling as capital goods, but they are accounted for in terms of energy requirement for their functioning. The life cycle impact assessment (LCIA) method employed is the EF 3.0, developed by the Joint Research Centre - European Commission (ref).<sup>80</sup> LCA calculations are performed with the software Simapro v.9.3.

From the LCA methodological perspective, the economic analysis is conducted following three cost items, namely, (i) the costs for the materials purchase, (ii) the cost for energy consumption, and (iii) the cost for the equipment, grounding on primary data about quantities and prices. The latter contribution is evaluated assuming a depreciation time of 10 years and an annual working time of 1760 h per year.<sup>50,86</sup> Based on this data, the annual depreciation cost of each tool is divided by the annual throughput, directly measured on the production line. The maintenance of the production line and the cost of human labor are not considered inside the system boundaries due to the uncertainty of these values in laboratory-scale activities.

#### ACKNOWLEDGEMENTS

This research was funded by the European Union's Horizon Europe Framework Programme, through a FET Proactive research and innovation action under grant agreement no. 101084124 (DIAMOND). The authors were supported by the European Union's Horizon 2020 Framework Programme for funding Research and Innovation under grant agreements no. 881603 (Graphene Flagship Core 3), no. 826013 (IMPRESSIVE), and no. 764047 (ESPReso). The authors acknowledge the project UNIQUE, supported under the umbrella of SOLAR-ERA.NET\_cofund by ANR, PtJ, MUR (GA 775970), MINECOAEI, SWEA, within the European Union Framework Program for Research and Innovation Horizon 2020 (Cofund ERANET Action, no. 691664). L. V and M.S. would like to thank Dr. Stefano Razza and Dr. Francesco Di Giacomo (University of Rome "Tor Vergata") for

fruitful discussions, and Dr. Francesca Zarotti (University of Rome “Tor Vergata”) for helpful assistance in XRD measurements.

## DATA AVAILABILITY STATEMENT

The data that support the findings of this study are openly available in Sub-module in ambient air at <https://10.17632/s84tsxdpjb.1>.

## ORCID

Luigi Vesce  <https://orcid.org/0000-0003-3322-8688>

Riccardo Basosi  <https://orcid.org/0000-0003-1026-7668>

Adalgisa Sinicropi  <https://orcid.org/0000-0001-5605-6482>

## REFERENCES

- Green MA, Dunlop ED, Hohl-Ebinger J, et al. Solar cell efficiency tables (version 60). *Prog Photovoltaics Res Appl*. 2022;30(7):687-701. doi:10.1002/pip.3595
- NREL, “Best Research-Cell Efficiency Chart,” can be found under. 2023. <https://www.nrel.gov/pv/cell-efficiency.html>
- Kojima A, Teshima K, Shirai Y, Miyasaka T. Organometal halide perovskites as visible-light sensitizers for photovoltaic cells. *J Am Chem Soc*. 2009;131(17):6050-6051. doi:10.1021/ja809598r
- Kim HS, Lee CR, Im JH, et al. Lead iodide perovskite sensitized all-solid-state submicron thin film mesoscopic solar cell with efficiency exceeding 9%. *Sci Rep*. 2012;2(1):1. doi:10.1038/srep00591
- Vesce L, Stefanelli M, Herterich JP, et al. Ambient air blade-coating fabrication of stable triple-cation perovskite solar modules by green solvent quenching. *Sol RRL*. 2021;5(8):1. doi:10.1002/solr.202100073
- NREL, “Champion Photovoltaic Module Efficiency Chart,” 2022.
- Feng SP, Cheng Y, Yip HL, et al. Roadmap on commercialization of metal halide perovskite photovoltaics. *J Phys Mater*. 2023;6. doi:10.1088/2515-7639/acc893
- Vesce L, Guidobaldi A, Mariani P, et al. Scaling-up of dye sensitized solar modules. *World Sci Ref Hybrid Mater*. 2019;423-485. doi:10.1142/9789813270541\_0013
- Lee D. K., Park N. G. Materials and methods for high-efficiency perovskite solar modules. *Sol RRL* 2021;2100455. doi:10.1002/solr.202100455.
- Ashworth C. Reproducible, high-performance perovskite solar cells. *Nat Rev Mater*. 2021;6(4):293. doi:10.1038/s41578-021-00310-2.
- Vesce L, Stefanelli M, Castriotta LA, et al. Hysteresis-free planar perovskite solar module with 19.1% efficiency by interfacial defects passivation. *Sol RRL*. 2022;6(7):2101095. doi:10.1002/solr.202101095
- Yang Z, Chueh CC, Zuo F, Kim JH, Liang PW, Jen AKY. High-performance fully printable perovskite solar cells via blade-coating technique under the ambient condition. *Adv Energy Mater*. 2015;5:1. doi:10.1002/aenm.201500328
- Motti SG, Meggiolaro D, Barker AJ, et al. Controlling competing photochemical reactions stabilizes perovskite solar cells. *Nat Photonics*. 2019;13(8):532-539. doi:10.1038/s41566-019-0435-1
- Yang M, Kim DH, Klein TR, et al. Highly efficient perovskite solar modules by scalable fabrication and interconnection optimization. *ACS Energy Lett*. 2018;3(2):322-328. doi:10.1021/acsenerylett.7b01221
- Bu T, Li J, Li H, et al. Lead halide-templated crystallization of methylamine-free perovskite for efficient photovoltaic modules. *Science (80-)*. 2021;372:1327. doi:10.1126/science.abh1035
- Liu C, Yang Y, Rakstys K, et al. Tuning structural isomers of phenylethylenediammonium to afford efficient and stable perovskite solar cells and modules. *Nat Commun*. 2021;12(1):1. doi:10.1038/s41467-021-26754-2
- Ding Y, Ding B, Kanda H, et al. Single-crystalline TiO<sub>2</sub> nanoparticles for stable and efficient perovskite modules. *Nat Nanotechnol*. 2022;17(6):598-605. doi:10.1038/s41565-022-01108-1
- Han GS, Kim J, Bae S, et al. Spin-coating process for 10 cm × 10 cm perovskite solar modules enabled by self-assembly of SnO<sub>2</sub> nanocolloids. *ACS Energy Lett*. 2019;4:1845. doi:10.1021/acsenerylett.9b00953
- Agresti A, Pescetelli S, Palma AL, et al. Two-dimensional material interface engineering for efficient perovskite large-area modules. *ACS Energy Lett*. 2019;4:1862. doi:10.1021/acsenerylett.9b01151
- Di Giacomo F, Shanmugam S, Fledderus H, et al. Up-scalable sheet-to-sheet production of high efficiency perovskite module and solar cells on 6-in. Substrate using slot die coating. *Sol Energy Mater sol Cells*. 2018;181:53-59. doi:10.1016/j.solmat.2017.11.010
- Deng Y, Ni Z, Palmstrom AF, et al. Reduced self-doping of perovskites induced by short annealing for efficient solar modules. *Joule*. 2020;4(9):1949-1960. doi:10.1016/j.joule.2020.07.003
- Deng Y, Xu S, Chen S, Xiao X, Zhao J, Huang J. Defect compensation in formamidinium-caesium perovskites for highly efficient solar mini-modules with improved photostability. *Nat Energy*. 2021;6(6):633-641. doi:10.1038/s41560-021-00831-8
- Chen S, Dai X, Xu S, Jiao H, Zhao L, Huang J. Stabilizing perovskite-substrate interfaces for high-performance perovskite modules. *Science (80-)*. 2021;373:902. doi:10.1126/science.abi6323
- Du M, Zhu X, Wang L, et al. High-pressure nitrogen-extraction and effective passivation to attain highest large-area perovskite solar module efficiency. *Adv Mater*. 2020;32(47):1. doi:10.1002/adma.202004979
- Deng Y, Zheng X, Bai Y, Wang Q, Zhao J, Huang J. Surfactant-controlled ink drying enables high-speed deposition of perovskite films for efficient photovoltaic modules. *Nat Energy*. 2018;3(7):560-566. doi:10.1038/s41560-018-0153-9
- Ding J, Han Q, Ge QQ, et al. Fully air-bladed high-efficiency perovskite photovoltaics. *Joule*. 2019;3(2):402-416. doi:10.1016/j.joule.2018.10.025
- Matteocci F, Vesce L, Kosasih FU, et al. Fabrication and morphological characterization of high-efficiency blade-coated perovskite solar modules. *ACS Appl Mater Interfaces*. 2019;11(28):25195-25204. doi:10.1021/acscami.9b05730
- Vesce L, Stefanelli M., Di Carlo A., 2019 *Int Symp Adv Electr Commun Technol* 2020, 764047, 1.
- Castriotta LA, Matteocci F, Vesce L, et al. Air-processed infrared-annealed printed methylammonium-free perovskite solar cells and modules incorporating potassium-doped graphene oxide as an interlayer. *ACS Appl Mater Interfaces*. 2021;13(10):11741-11754. doi:10.1021/acscami.0c18920
- Green MA, Hishikawa Y, Dunlop ED, Levi DH, Hohl-Ebinger J, Ho-Baillie AWY. Solar cell efficiency tables (version 52). *Prog Photovoltaics Res Appl*. 2018;26(7):427-436. doi:10.1002/pip.3040
- Bu T, Ono LK, Li J, et al. Modulating crystal growth of formamidinium-caesium perovskites for over 200 cm<sup>2</sup> photovoltaic sub-modules. *Nat Energy*. 2022;7(6):528-536. doi:10.1038/s41560-022-01039-0
- Patidar R, Burkitt D, Hooper K, Richards D, Watson T. Slot-die coating of perovskite solar cells: an overview. *Mater Today Commun*. 2020;22:100808. doi:10.1016/j.mtcomm.2019.100808
- Daniel Burkitt TW, Greenwood P, Hooper K, et al. Meniscus guide slot-die coating for roll-to-roll perovskite solar cells. *MRS Adv*. 2019;357:1.
- Vesce L, Riccitelli R. Processing and characterization of a TiO<sub>2</sub> paste based on small particle size powders for dye-sensitized solar cell semi-transparent photo-electrodes. *Prog Photovoltaics Res Appl*. 2012;20(8):960-966. doi:10.1002/pip.1166
- Kim H-J, Kim H-S, Park N-G. Progress of perovskite solar modules. *Adv Energy Sustain Res*. 2021;2(6):2000051. doi:10.1002/aesr.202000051
- Singh T, Miyasaka T. Stabilizing the efficiency beyond 20% with a mixed cation perovskite solar cell fabricated in ambient air under

- controlled humidity. *Adv Energy Mater.* 2018;8:1. doi:10.1002/aenm.201700677
37. Baxter JB, Vac J. Commercialization of dye sensitized solar cells: present status and future research needs to improve efficiency, stability, and manufacturing. *Sci Technol A Vacuum, Surfaces, Film.* 2012;30:020801. doi:10.1116/1.3676433
  38. Späth M, Sommeling PM, Van Roosmalen JAM, et al. Reproducible manufacturing of dye-sensitized solar cells on a semi-automated baseline. *Prog Photovoltaics Res Appl.* 2003;11(3):207-220. doi:10.1002/pip.481
  39. Mincuzzi G, Vesce L, Schulz-Ruhtenberg M, et al. Taking temperature processing out of dye-sensitized solar cell fabrication: fully laser-manufactured devices. *Adv Energy Mater.* 2014;4(14):1. doi:10.1002/aenm.201400421
  40. Parisi ML, Maranghi S, Vesce L, Sinicropi A, Di Carlo A, Basosi R. Prospective life cycle assessment of third-generation photovoltaics at the pre-industrial scale: a long-term scenario approach. *Renew Sustain Energy Rev.* 2020;121:109703. doi:10.1016/j.rser.2020.109703
  41. Laurent A, Espinosa N, Hauschild MZ. LCA of energy systems. In: Hauschild MZ, Rosenbaum RK, Olsen SI, eds. *Life Cycle Assessment: Theory and Practice.* Springer International Publishing; 2018:633-668. doi:10.1007/978-3-319-56475-3\_26
  42. Muteri V, Cellura M, Curto D, et al. Review on life cycle assessment of solar photovoltaic panels. *Energies.* 2020;13. doi:10.3390/en13010252
  43. Rossi F, Parisi ML, Maranghi S, Basosi R, Sinicropi A. Environmental analysis of a nano-grid: a life cycle assessment. *Sci Total Environ.* 2020;700:134814. doi:10.1016/j.scitotenv.2019.134814
  44. Arvidsson R, Tillman AM, Sandén BA, et al. Environmental assessment of emerging technologies: recommendations for prospective LCA. *J Ind Ecol.* 2018;22(6):1286-1294. doi:10.1111/jiec.12690
  45. Fthenakis VM, Kim HC. Photovoltaics: life-cycle analyses. *Sol Energy.* 2011;85(8):1609-1628. doi:10.1016/j.solener.2009.10.002
  46. Asdrubali F, Baldinelli G, D'Alessandro F, Scrucca F. Life cycle assessment of electricity production from renewable energies: review and results harmonization. *Renew Sustain Energy Rev.* 2015;42:1113-1122. doi:10.1016/j.rser.2014.10.082
  47. Maranghi S, Brondi C. *Life Cycle Assessment in the Chemical Product Chain: Challenges, Methodological Approaches and Applications.* Springer International Publishing; 2020. doi:10.1007/978-3-030-34424-5
  48. Maranghi S, Parisi ML, Basosi R, Sinicropi A. Environmental profile of the manufacturing process of perovskite photovoltaics: harmonization of life cycle assessment studies. *Energies.* 2019;12(19):3746. doi:10.3390/en12193746
  49. Zhang J, Chang N, Fagerholm C, et al. Techno-economic and environmental sustainability of industrial-scale productions of perovskite solar cells. *Renew Sustain Energy Rev.* 2022;158:112146. doi:10.1016/j.rser.2022.112146
  50. Song Z, McElvany CL, Phillips AB, et al. A techno-economic analysis of perovskite solar module manufacturing with low-cost materials and techniques. *Energ Environ Sci.* 2017;10(6):1297-1305. doi:10.1039/C7EE00757D
  51. Chen W, Chen H, Xu G, et al. Precise control of crystal growth for highly efficient CsPbI<sub>2</sub>Br perovskite solar cells. *Joule.* 2019;3(1):191-204. doi:10.1016/j.joule.2018.10.011
  52. Saliba M, Correa-Baena JP, Wolff CM, et al. How to make over 20% efficient perovskite solar cells in regular (n-i-p) and inverted (p-i-n) architectures. *Chem Mater.* 2018;30(13):4193-4201. doi:10.1021/acs.chemmater.8b00136
  53. Li D, Zhang D, Lim KS, et al. A review on scaling up perovskite solar cells. *Adv Funct Mater.* 2021;31(12):1. doi:10.1002/adfm.202008621
  54. Mariani P, Vesce L, Di Carlo A. The role of printing techniques for large-area dye sensitized solar cells. *Semicond Sci Technol.* 2015;30(10):104003. doi:10.1088/0268-1242/30/10/104003
  55. Whitaker JB, Kim DH, Larson BW, et al. Scalable slot-die coating of high performance perovskite solar cells. *Sustain Energy Fuel.* 2018;2(11):2442-2449. doi:10.1039/C8SE00368H
  56. Liu K, Liang Q, Qin M, et al. Zwitterionic-surfactant-assisted room-temperature coating of efficient perovskite solar cells. *Joule.* 2020;4(11):2404-2425. doi:10.1016/j.joule.2020.09.011
  57. Abdi-Jalebi M, Andaji-Garmaroudi Z, Pearson AJ, et al. Potassium- and rubidium-passivated alloyed perovskite films: optoelectronic properties and moisture stability. *ACS Energy Lett.* 2018;3(11):2671-2678. doi:10.1021/acsenergylett.8b01504
  58. Suo J, Yang B, Hagfeldt A. Passivation strategies through surface reconstruction toward highly efficient and stable perovskite solar cells on nip architecture. *Energies.* 2021;14(16):4836. doi:10.3390/en14164836
  59. Zhu H, Liu Y, Eickemeyer FT, et al. Tailored amphiphilic molecular mitigators for stable perovskite solar cells with 23.5% efficiency. *Adv Mater.* 2020;32(12):1. doi:10.1002/adma.201907757
  60. Zheng X, Chen B, Dai J, et al. Defect passivation in hybrid perovskite solar cells using quaternary ammonium halide anions and cations. *Nat Energy.* 2017;2(7):17102. doi:10.1038/nenergy.2017.102
  61. Yoshikawa K, Kawasaki H, Yoshida W, et al. Silicon heterojunction solar cell with interdigitated back contacts for a photoconversion efficiency over 26%. *Nat Energy.* 2017;2(5):17032. doi:10.1038/nenergy.2017.32
  62. Yoo MR, Seo JJ, Chua G. Efficient perovskite solar cells via improved carrier management. *Nature.* 2021;590(7847):587-593. doi:10.1038/s41586-021-03285-w
  63. Jiang Q, Zhao Y, Zhang X, et al. Surface passivation of perovskite film for efficient solar cells. *Nat Photonics.* 2019;13(7):460-466. doi:10.1038/s41566-019-0398-2
  64. Chen P, Bai Y, Wang S, Lyu M, Yun JH, Wang L. In situ growth of 2D perovskite capping layer for stable and efficient perovskite solar cells. *Adv Funct Mater.* 2018;28(17):1. doi:10.1002/adfm.201706923
  65. Chen J, Park NG. Materials and methods for Interface engineering toward stable and efficient perovskite solar cells. *ACS Energy Lett.* 2020;5(8):2742-2786. doi:10.1021/acsenergylett.0c01240
  66. Liang Q, Liu K, Sun M, et al. Manipulating crystallization kinetics in high-performance blade-coated perovskite solar cells via cosolvent-assisted phase transition. *Adv Mater.* 2022;34. doi:10.1002/adma.202200276
  67. Xie L, Cho AN, Park NG, Kim K. Efficient and reproducible CH<sub>3</sub>NH<sub>3</sub>PbI<sub>3</sub> perovskite layer prepared using a binary solvent containing a cyclic urea additive. *ACS Appl Mater Interfaces.* 2018;10(11):9390-9397. doi:10.1021/acsami.7b18761
  68. Noel NK, Habisreutinger SN, Wenger B, et al. A low viscosity, low boiling point, clean solvent system for the rapid crystallisation of highly specular perovskite films. *Energ Environ Sci.* 2017;10(1):145-152. doi:10.1039/C6EE02373H
  69. Liu J, Wang D, Zhang Y, et al. Room-temperature-processed, carbon-based fully printed mesoscopic perovskite solar cells with 15% efficiency. *Sol RRL.* 2021;5(8):2100274. doi:10.1002/solr.202100274
  70. Huang HH, Liu QH, Tsai H, et al. A simple one-step method with wide processing window for high-quality perovskite mini-module fabrication. *Joule.* 2021;5(4):958-974. doi:10.1016/j.joule.2021.02.012
  71. Deng Y, van Brackle CH, Dai X, Zhao J, Chen B, Huang J. Tailoring solvent coordination for high-speed, room-temperature blading of perovskite photovoltaic films. *Sci Adv.* 2019;5(12):1. doi:10.1126/sciadv.aax7537
  72. Li H, Xia Y, Wang C, et al. High-efficiency and stable perovskite solar cells prepared using chlorobenzene/acetonitrile antisolvent. *ACS Appl Mater Interfaces.* 2019;11(38):34989-34996. doi:10.1021/acsami.9b12323
  73. Dunbar RB, Duck BC, Moriarty T, et al. How reliable are efficiency measurements of perovskite solar cells? The first inter-comparison,

- between two accredited and eight non-accredited laboratories. *J Mater Chem A*. 2017;5(43):22542-22558. doi:[10.1039/C7TA05609E](https://doi.org/10.1039/C7TA05609E)
74. Sadhanala A, Kumar A, Pathak S, et al. Electroluminescence from organometallic lead halide perovskite-conjugated polymer diodes. *Adv Electron Mater*. 2015;1(3):1. doi:[10.1002/aelm.201500008](https://doi.org/10.1002/aelm.201500008)
  75. LaMer VK, Dinegar RH. Theory, production and mechanism of formation of monodispersed hydrosols. *J Am Chem Soc*. 1950;72(11):4847-4854. doi:[10.1021/ja01167a001](https://doi.org/10.1021/ja01167a001)
  76. Hu H, Singh M, Wan X, Tang J, Chu CW, Li G. Nucleation and crystal growth control for scalable solution-processed organic-inorganic hybrid perovskite solar cells. *J Mater Chem a*. 2020;8(4):1578-1603. doi:[10.1039/C9TA11245F](https://doi.org/10.1039/C9TA11245F)
  77. Khenkin MV, Katz EA, Abate A, et al. Consensus statement for stability assessment and reporting for perovskite photovoltaics based on ISOS procedures. *Nat Energy*. 2020;5:35. doi:[10.1038/s41560-019-0529-5](https://doi.org/10.1038/s41560-019-0529-5)
  78. Domanski K, Alharbi EA, Hagfeldt A, Grätzel M, Tress W. Systematic investigation of the impact of operation conditions on the degradation behaviour of perovskite solar cells. *Nat Energy*. 2018;3(1):61-67. doi:[10.1038/s41560-017-0060-5](https://doi.org/10.1038/s41560-017-0060-5)
  79. Palma AL. Laser-processed perovskite solar cells and modules. *Sol RRL*. 2020;4(4):1. doi:[10.1002/solr.201900432](https://doi.org/10.1002/solr.201900432)
  80. Fazio S, Castellani V, Sala S, et al. *Supporting Information to the Characterisation Factors of Recommended EF Life Cycle Impact Assessment Methods: New Methods and Differences with ILCD*, 2018.
  81. Rong Y, Ming Y, Ji W, et al. Toward industrial-scale production of perovskite solar cells: screen printing, slot-die coating, and emerging techniques. *J Phys Chem Lett*. 2018;9(10):2707-2713. doi:[10.1021/acs.jpcllett.8b00912](https://doi.org/10.1021/acs.jpcllett.8b00912)
  82. International Organization for Standardization, ISO 14040:2006 – Environmental management: life cycle assessment: principles and framework, n.d.
  83. International Organization for Standardization, ISO 14044:2006 – Environmental management—life cycle assessment—requirements, 2006.
  84. E. C. Joint Research Centre, *ILCD Handbook - Framework and Requirements for LCIA Models and Indicators First Edition*, 2010.
  85. Wernet G, Bauer C, Steubing B, Reinhard J, Moreno-Ruiz E, Weidema B. The ecoinvent database version 3 (part I): overview and methodology. *Int J Life Cycle Assess*. 2016;21(9):1218-1230. doi:[10.1007/s11367-016-1087-8](https://doi.org/10.1007/s11367-016-1087-8)
  86. “OECD Employment Outlook,” can be found under. 2021. <http://www.oecd.org/employment-outlook/>

## SUPPORTING INFORMATION

Additional supporting information can be found online in the Supporting Information section at the end of this article.

**How to cite this article:** Vesce L, Stefanelli M, Rossi F, et al. Perovskite solar cell technology scaling-up: Eco-efficient and industrially compatible sub-module manufacturing by fully ambient air slot-die/blade meniscus coating. *Prog Photovolt Res Appl*. 2023;1-15. doi:[10.1002/pip.3741](https://doi.org/10.1002/pip.3741)